



# Iron as recyclable energy carrier: Feasibility study and kinetic analysis of iron oxide reduction

C. Kuhn<sup>a</sup>, A. Düll<sup>a</sup>, P. Rohlf<sup>a</sup>, S. Tischer<sup>b</sup>, M. Börnhorst<sup>a</sup>, O. Deutschmann<sup>a,b,\*</sup>

<sup>a</sup> Institute for Chemical Technology and Polymer Chemistry, Karlsruhe Institute of Technology (KIT), Kaiserstr. 12, 76131 Karlsruhe, Germany

<sup>b</sup> Institute of Catalysis Research and Technology, Karlsruhe Institute of Technology (KIT), Kaiserstr. 12, 76131 Karlsruhe, Germany

## ARTICLE INFO

### Keywords:

Metal fuels  
Iron  
Cycle efficiency  
Reduction  
Kinetics

## ABSTRACT

Carbon-free and sustainable energy storage solutions are required to mitigate climate change. One possible solution, especially for stationary applications, could be the storage of energy in metal fuels. Energy can be stored through reduction of the oxide with green hydrogen and be released by combustion. In this work a feasibility study for iron as possible metal fuel considering the complete energy cycle is conducted. On the basis of equilibrium calculations it could be shown that the power-to-power efficiency of the iron/iron oxide cycle is 27%. As technology development requires a more detailed description of both the reduction and the oxidation, a first outlook is given on the kinetic analysis of the reduction of iron oxides with hydrogen. Thermogravimetric experiments using Fe<sub>2</sub>O<sub>3</sub>, Fe<sub>3</sub>O<sub>4</sub> and FeO indicate a three-step process for the reduction. The maximum reduction rate can be achieved with a hydrogen content of 25%. Based on the experimental results a reaction mechanism and accompanied kinetic data were developed for description of Fe<sub>2</sub>O<sub>3</sub> reduction with H<sub>2</sub> under varying experimental conditions.

## 1. Introduction

To minimize the impact of the climate crisis, the Paris Climate Agreement was adopted in 2015, calling for limitation of the average global temperature increase to 1.5 °C above pre-industrial levels [1]. This requirement was reaffirmed at COP26 in Glasgow, emphasizing that achieving the 1.5 °C goal will require net zero CO<sub>2</sub> emissions around mid-century [2]. The achievement of this goal implies the transformation of the energy sector worldwide from fossil fuels to renewable energies. One of the key challenges is to replace coal-fired power plants as one third of the world's electricity generation is based on coal being responsible for 30% of global CO<sub>2</sub> emissions [3,4]. A stable supply based solely on renewable energies, e.g. solar and wind, must meet high demands. The production of energy from renewable resources will most likely be concentrated in places with high solar radiation or wind and underlies temporal and seasonal fluctuations. Thus, energy storage solutions are necessary which enable long-term storage, safe and easy global transportation as well as the possibility of large-scale application. Energy storage technologies include batteries, thermal and mechanical energy storage, or synthetic fuels. The suitability of energy carriers differs depending on application and requirements. Batteries, for example, have a very high efficiency (70% to 90% [5]), but are only suitable for short-term storage due to their capacity [6]. Green

hydrogen, produced via electrolysis with electricity from renewable resources, is one widely discussed energy carrier to replace fossil fuels due to its high specific energy (33 kWh kg<sup>-1</sup> [7]). However, its usage as large-scale application for energy storage is limited due to its low volumetric energy density requiring liquefaction or compression for transportation resulting in a decrease of system efficiency [8,9].

Metal fuels are energy carriers that meet the requirements of safe and easy transportation, long-term storage and high energy density [10–12]. First studies have been published that investigated metal fuels as energy carrier regarding cycle efficiency [10,11,13–16]. Trowell et al. [16] investigated the efficiency of aluminium as energy carrier. They state a cycle efficiency of 25% based on rough assumptions for oxidation (heat engine with 40% efficiency) and reduction (based on the energy required for primary Al production) [16]. For silicon, Auner and Holl [11] state a storage efficiency factor of nearly 30%. Assuming strong technology development, efficiencies of up to 40% are predicted [10]. The metal powder is combusted releasing energy and forming solid metal oxides which can be easily collected. Recycling of the metal oxides is performed in areas, where sufficient and cheap green energy is available. These processes can be combined to a sustainable energy cycle, which meets the requirements of a carbon-free energy carrier and the circular economy. A proposed scheme is shown

\* Corresponding author at: Institute for Chemical Technology and Polymer Chemistry, Karlsruhe Institute of Technology (KIT), Kaiserstr. 12, 76131 Karlsruhe, Germany.

E-mail address: [deutschmann@kit.edu](mailto:deutschmann@kit.edu) (O. Deutschmann).

<https://doi.org/10.1016/j.jaecs.2022.100096>

Received 23 May 2022; Received in revised form 9 September 2022; Accepted 31 October 2022

Available online 8 November 2022

2666-352X/© 2022 The Author(s). Published by Elsevier Ltd. This is an open access article under the CC BY license (<http://creativecommons.org/licenses/by/4.0/>).

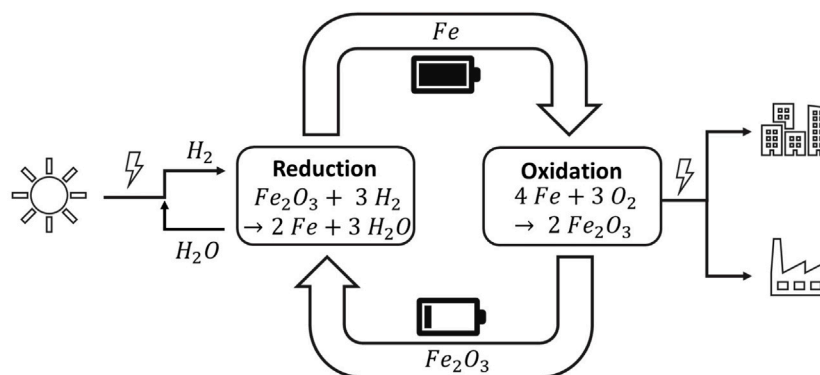


Fig. 1. Proposed energy cycle for iron as recyclable metal fuel. The reduction of iron oxides, which equals the energy storage process, will be conducted in areas with excess of renewable energies. The obtained iron powder will be transported to areas where energy is required, e.g. populated or industrial areas. Iron is combusted and electricity is produced with a heat engine. The collected iron oxide powder can then be returned and recycled.

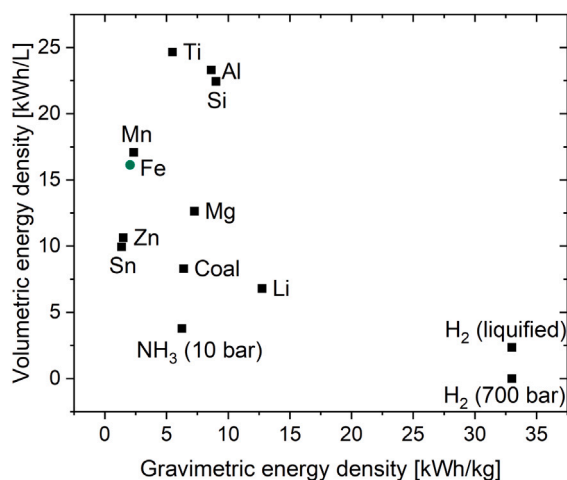


Fig. 2. Volumetric and gravimetric energy densities of possible metals fuels [19], coal [20], ammonia [21] and hydrogen [7,22].

in Fig. 1. Attractive candidates for metal fuels are aluminium, silicon and iron due to their non-toxicity and high occurrence in the earth's crust [17,18]. The gravimetric and volumetric energy densities of potential metal fuels in comparison to coal and hydrogen are given in Fig. 2.

In terms of volumetric energy density, metal fuels perform very well compared to hydrogen. Compared to coal, the volumetric energy density is comparable (Zn, Sn) or higher (Fe, Si, Al). Regarding the gravimetric energy density, aluminium ( $8.6 \text{ kWh kg}^{-1}$ ) and silicon ( $9 \text{ kWh kg}^{-1}$ ) are comparable to coal ( $6.4 \text{ kWh kg}^{-1}$ ), while the energy density of iron is lower ( $2.1 \text{ kWh kg}^{-1}$ ) [19]. Another crucial factor is the oxidation [23]. It was shown that iron combusts heterogeneously without forming metal vapour and nanoparticles, which enables effective separation of the oxidation product [23–25]. In comparison to iron, aluminium is predicted to combust under the formation of a vapour phase leading to nanometric solid metal oxide products [23]. Additionally, it was proposed that with a burning velocity comparable to hydrocarbons and the similarities of metal powders and pulverized coal, retrofitted coal-fired power plants can be used for power generation through metal combustion [23,24]. Closing the cycle by  $\text{CO}_2$ -free reduction of the metal oxides is decisive for a sustainable energy system. Although current research focuses on alternatives for the carbon- and energy intense reduction processes for aluminium and silicon, development does not yet exceed laboratory scale [11,18,26,27]. Here, electrolysis for metal production is of particular interest, since no additional intermediate step, e.g. production of the reductant, is required,

which would increase the efficiency [10,28–30]. The production of iron via the electrochemical route is a current topic in research [31,32]. One of the major challenges is the dissolution of iron oxides. Beside the low temperature electrolysis in alkaline solution, the electrolysis in ionic liquids is discussed [33,34]. However, the reduction of iron oxides with green hydrogen is a key factor for reducing  $\text{CO}_2$  emissions in the steel industry and proven to be applicable in large-scale [35–38], even though retrofitted steel plants with internal dry reforming processes seem to be more promising in the very near future [39]. Considering the advantages that iron has in terms of combustion and recycling, this work focuses on iron as potential metal fuel.

The reduction of iron oxide ( $\text{Fe}_2\text{O}_3$ ) is a complex multistep reaction over different intermediates ( $\text{Fe}_3\text{O}_4$ ,  $\text{FeO}$ ). A more detailed understanding is of high interest in various applications, e.g. steel industry, chemical looping or catalysis [40–42]. Numerous works focus on the elucidation of the reaction kinetics and the underlying reaction mechanism based on thermogravimetric analysis (TGA) or temperature programmed reduction (TPR) [43–46]. Pineau et al. [47] state that the reaction mechanism is a function of temperature. At temperatures below  $420^\circ\text{C}$  iron oxide reduction is proposed to be a two-step mechanism with  $\text{Fe}_3\text{O}_4$  as intermediate. At temperatures above  $570^\circ\text{C}$   $\text{FeO}$  is additionally formed before complete reduction to  $\text{Fe}$  [47]. For temperatures above  $700^\circ\text{C}$  Wang et al. [42] showed that the reduction  $\text{Fe}_2\text{O}_3 \rightarrow \text{Fe}_3\text{O}_4$  and  $\text{Fe}_3\text{O}_4 \rightarrow \text{FeO}$  proceed simultaneously, thus the overall reduction can be seen as a two-step process  $\text{Fe}_2\text{O}_3 \rightarrow \text{FeO} \rightarrow \text{Fe}$ . Lee et al. [48] investigated the non-isothermal reduction of  $\text{Fe}_2\text{O}_3$  nanoparticles. They demonstrated that the reduction steps take place consecutively and no  $\text{FeO}$  is formed as the reduction is completed below  $570^\circ\text{C}$ . This indicates that the crucial point of the reduction mechanism is the occurrence and stability of  $\text{FeO}$ . Thus, for a detailed understanding of the reduction mechanism, investigations regarding the reduction of the oxides  $\text{FeO}$  and  $\text{Fe}_3\text{O}_4$  are decisive. Experiments on the reduction of the three oxide species were performed by Jozwiak et al. [41]. They conducted TPR measurements of  $\text{Fe}_2\text{O}_3$ ,  $\text{Fe}_3\text{O}_4$  and  $\text{FeO}$  with 5%  $\text{H}_2$  in Ar accompanied by in-situ XRD. In contrast to the publications listed above a three-stage mechanism with  $\text{Fe}_3\text{O}_4$  and  $\text{FeO}$  as intermediate species independent from temperature was postulated. For temperatures below  $570^\circ\text{C}$  the mechanism is extended to include the disproportionation of wüstite ( $\text{FeO} \rightleftharpoons \text{Fe}_3\text{O}_4 + \text{Fe}$ ) [41]. Although several studies investigate the reduction of iron oxides, the influence of varying hydrogen content has hardly been described. Wang et al. [42] studied the isothermal reduction of  $\text{Fe}_2\text{O}_3$  with hydrogen contents from 10% to 40%. They state that the reaction rate increases linearly with increasing  $\text{H}_2$  content. Kinetics of gas–solid reactions such as the reduction of  $\text{Fe}_2\text{O}_3$  with hydrogen are normally described with a function describing the reaction process as a kinetic model, e.g. diffusion-controlled or boundary-controlled [47,49]. The kinetic models describing solid-state processes are not based on classical reaction equations relying on





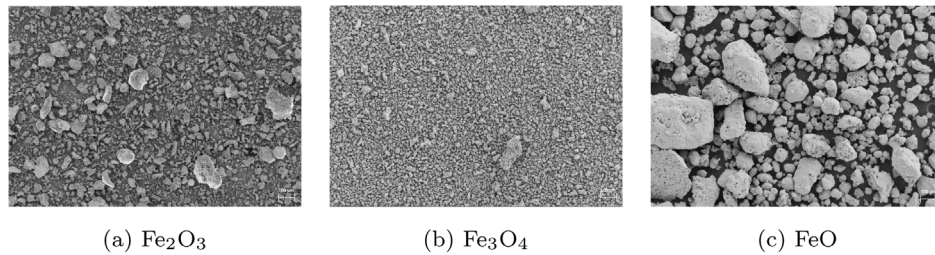


Fig. 5. SEM images of (a)  $\text{Fe}_2\text{O}_3$  (b)  $\text{Fe}_3\text{O}_4$  and (c)  $\text{FeO}$  before milling.

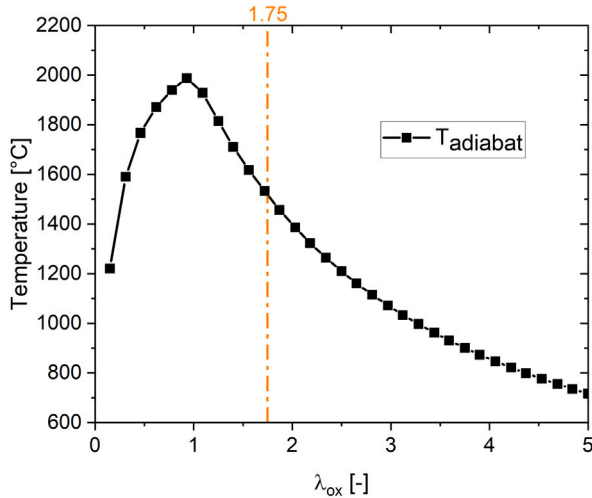


Fig. 6. Adiabatic combustion temperature of iron in dependence of the air-to-fuel ratio  $\lambda_{\text{ox}}$ . For  $\lambda_{\text{ox}} > 1.75$  is the adiabatic combustion temperature below the melting points of the occurring oxides.

### 3.1. Oxidation

One of the main advantages of iron as recyclable metal fuel is the possibility of retrofitting coal-fired power plants which would greatly lower the hurdles for the introduction of the new technology [23,24]. The main parts that could remain would be the fuel-burning section and the steam turbine cycle [61]. Thus, the oxidation process is modelled based on data of a modern coal-fired power plant (RDK-8, Karlsruhe, Germany [50,52]). In contrast to coal-fired power plants, the combustion of iron particles leads to solid oxidation products ( $\text{Fe}_2\text{O}_3$ ). This requires modifications of the process in terms of particle collection devices (s. Fig. 3). Although not considered in this work, it is interesting that the required exhaust gas aftertreatment systems would be less complex for iron-fired power plants, since only  $\text{NO}_x$  formation might be a severe problem [61]. Melting and agglomeration of the iron and iron oxide particles must be considered as it might lead to blockages and deposits in the reactor or on the reactor walls. Depending on the reactor design of the reduction and oxidation processes, another objective might be to oxidize and reduce iron and iron oxide particles without intermediate adjustment of the particle sizes, which would lower the cycle efficiency. To prevent melting and agglomeration of the particles the oxidation temperature should not exceed the melting temperature of iron ( $T_m = 1530^\circ\text{C}$  [54]) and its main oxidation product ( $\text{Fe}_2\text{O}_3$ ,  $T_m = 1560^\circ\text{C}$  [54]).

Thus, the dependence of the adiabatic combustion temperature on the air-to-fuel ratio ( $\lambda_{\text{ox}}$ ) was determined (Fig. 6). At stoichiometric conditions ( $\lambda_{\text{ox}} = 1$ ) iron reaches an adiabatic combustion temperature of  $2004^\circ\text{C}$ . As can be depicted from Fig. 6, the adiabatic combustion temperature decreases with further increasing  $\lambda_{\text{ox}}$ . For  $\lambda_{\text{ox}} > 1.75$  is the combustion temperature below the melting temperature of iron and

iron oxide ( $\text{Fe}_2\text{O}_3$ ). Taking into account that the reactant stream is preheated, the air-to-fuel-ratio may be increased to  $\lambda_{\text{ox}} = 2$  to realize an adiabatic combustion temperature below the melting points of  $\text{Fe}$  and  $\text{Fe}_2\text{O}_3$ . Another advantage of the combustion with an excess of oxygen might be the avoidance of nanoparticle formation as postulated by Tóth et al. [25].

Based on the specifications, i.e.  $\lambda_{\text{ox}} = 2$  and a net electricity output of  $843\text{ MW}$  ( $P_{\text{el}}$ ), which is specified by the model steam turbine [50,52], the oxidation efficiency is calculated:

$$\eta_{\text{ox}} = \frac{P_{\text{el}}}{\dot{m}_{\text{Fe}} \cdot HV_{\text{Fe}}} \quad (7)$$

The iron feed stream of  $\dot{m}_{\text{Fe}} = 263\text{ kg s}^{-1}$  is calculated to supply the necessary heat to the steam turbine cycle of RDK-8.  $HV_{\text{Fe}}$  is the heating value of iron ( $7385\text{ kJ kg}^{-1}$  [19]). The efficiency of the oxidation process is 43 %.

### 3.2. Reduction

In the first step, the optimum operating parameters for iron oxide reduction with hydrogen were determined. Various equilibrium calculations were carried out at different temperatures and hydrogen ratios ( $\lambda_{\text{red}}$ ). Fig. 7(a) shows the dependence of the iron yield on the temperature for varying hydrogen ratios. At stoichiometric conditions ( $\lambda_{\text{red}} = 1$ ) the maximum iron yield achievable at  $1000^\circ\text{C}$  is 40 %. An increase of the hydrogen content to  $\lambda_{\text{red}} = 2$  results in a significant increase of the iron yield. Here, complete reduction is reached at  $900^\circ\text{C}$ . A hydrogen ratio of  $\lambda_{\text{red}} = 3$  results in a complete reduction at  $800^\circ\text{C}$ . As can be depicted from Fig. 7(a) and (b) further increasing the hydrogen content shows only smaller effects on the yield or the reduction temperature.

Based on the request of nearly 100 % iron yield and an appropriate hydrogen ratio, possible operating points were determined. Due to the very high temperatures required for reduction, hydrogen ratios of less than  $\lambda_{\text{red}} = 2$  are not economically interesting. At the same time, an increase of  $\lambda_{\text{red}}$  to values above 3 leads only to a slight decrease of the reduction temperature and causes technical disadvantages due to the high volume flux. Thus, in this work two possible operating points are compared. A hydrogen ratio of  $\lambda_{\text{red}} = 2.8$  at a reduction temperature of  $900^\circ\text{C}$  (case 1) and a hydrogen ratio of  $\lambda_{\text{red}} = 3$  at a reduction temperature of  $800^\circ\text{C}$  (case 2). Reduction efficiency is calculated according to Eq. (8), where  $HV_{\text{Fe}}$  is the heating value of iron ( $7385\text{ kJ kg}^{-1}$  [19]),  $\dot{m}_{\text{Fe}}$  the resulting iron stream and  $\Delta E_{\text{red}}$  the energy required for reduction [13].

$$\eta_{\text{red}} = \frac{\dot{m}_{\text{Fe}} \cdot HV_{\text{Fe}}}{\Delta E_{\text{red}}} \quad (8)$$

The two cases and the resulting efficiencies are compared in Table 5. The reduction efficiency of case 2  $\eta_{\text{red}} = 0.75$  is slightly larger than for case 1 with  $\eta_{\text{red}} = 0.73$ . Again, heat recovery plays a crucial role for the process efficiency. Assuming optimum heat recovery increases the efficiency to  $\eta_{\text{red,opt}} = 0.91$  (case 2) or  $\eta_{\text{red,opt}} = 0.90$  (case 1). Heat recovery is realized with a regenerator (Fig. 4). Depending on the particle size and process design, the resulting iron particles can

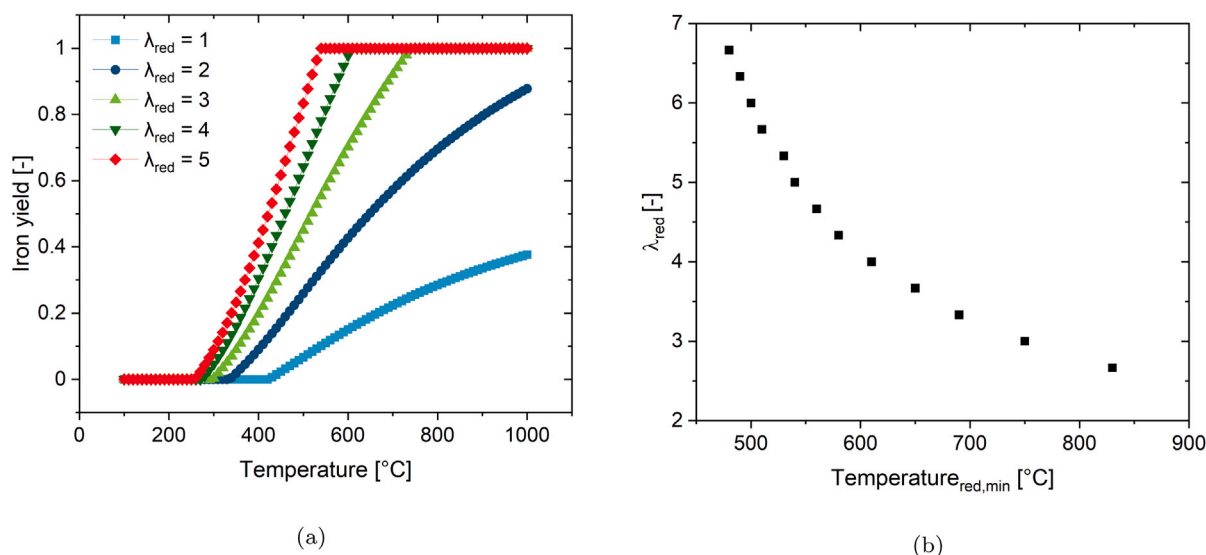


Fig. 7. (a) Iron yield of the reduction depending on the hydrogen ratio and the temperature and (b) minimum reduction temperature ( $T_{red,min}$ ) for complete reduction in dependence on the hydrogen ratio ( $\lambda_{red}$ ).

Table 5  
Comparison of the reduction cases.

	Case 1	Case 2
Reduction temperature [°C]	900	800
Hydrogen ratio $\lambda_{red}$	2.8	3
Efficiency $\eta_{red}$	0.73	0.75
Efficiency with optimum heat recovery $\eta_{red,opt}$	<b>0.90</b>	<b>0.91</b>

be separated from the gas stream before or after the heat recovery system. For larger particle sizes ( $d > 20 \mu\text{m}$ ) a cyclone can be used [56]. Cyclones allow operation at high temperatures and particle separation before the regenerator. Smaller particle sizes require an electrostatic filter which cannot be operated at high temperatures [51,56]. Thus, the electrostatic filter needs to be downstream of the heat recovery system. Decreasing the temperature of the gas flux containing the iron particles might lead to a decrease in the iron yield according to the equilibrium calculations (s. Fig. 7(a)). Here, both the kinetics of the back reaction and the residence time determine how strongly the iron yield is depleted. Due to a lack of data regarding the kinetics of iron oxidation with water vapour this was not considered in this work. Nevertheless, this is an important question that needs to be addressed in future research.

### 3.3. Cycle efficiency

Assuming efficiencies of  $\eta_{ox} = 0.43$  for the oxidation and  $\eta_{red} = 0.91$  ( $\lambda_{red} = 3$ ,  $T_{red} = 800^\circ\text{C}$ ) for the reduction process, the efficiency of the energy storage cycle is 39% for the optimum case. With additional consideration of hydrogen electrolysis efficiency (70% [62]) an overall power-to-power efficiency of 27% is calculated. In this work the processes required for energy storage and energy release are considered. For a more detailed description of the overall cycle, the costs and energy losses due to transportation need to be taken into account as well. Here, the fact that oxidation leads to 43% increase in weight should not be neglected. For the combustion process micron-sized iron particles will be required [10,23]. Thus, depending on the design of the reduction process an additional milling step might be necessary, which would lower the efficiency. When considering multiple storage and retrieval cycles, additional effects such as material losses, incomplete reduction or oxidation and storage losses might have an effect as well and are recommended to be considered in a more detailed case study

in future investigations. To better contextualize the efficiency of the iron cycle, it is helpful to compare it to other carbon-free energy carrier, for example ammonia or hydrogen. For liquid hydrogen the following steps are assumed to determine the power-to-power efficiency [63]: Hydrogen production (70% [62]), hydrogen liquefaction (55% to 73% [64]) and power generation via fuel cell (60% [65,66]) or combined combustion (55% to 60% [67,68]). This results in power-to-power efficiencies of 21% to 31%. For  $\text{CO}_2$ -free ammonia production hydrogen production via electrolysis and cryogenic air separation for nitrogen supply is assumed. Here, power consumption ranging from  $7 \text{ kWh kg}^{-1}$  to  $11 \text{ kWh kg}^{-1}$  is postulated, which results in power-to-ammonia efficiencies from 47% to 74% [68,69]. With power generation via fuel cell (56% to 57% [70]) or combined combustion (55% to 60% [67,68]) power-to-power efficiencies of 26% to 44% are calculated. It should be noted, that for hydrogen and ammonia the effects of storage and transportation (e.g. boil-off or cooling [63]) are not considered in the calculated efficiencies as well, since here a detailed case study would be required. The comparison with hydrogen and ammonia shows that iron can certainly be considered as a possible energy carrier. However, it also shows that it is not the efficiency of the process that is the decisive advantage, but rather the good handling capability and the possibility of using existing structures [61]. The comparison with conventional energy sources seems disillusioning at first glance. The RDK-8, operated with hard coal, achieves an efficiency of 46% [71]. However, this efficiency only takes power generation into account. For a holistic view, external costs, e.g. for carbon capture and storage (CCS), would also have to be considered, which would significantly diminish efficiency. A review paper by Goto et al. [72] claims an efficiency penalty of around 10% by adding CCS to existing coal-fired power plants. This shows that iron meets the requirements of an energy storage system for stationary applications. The presented study is an initial evaluation of iron as metal fuel and inevitably subject to many simplifications. Even though there has been a strong increase in research in recent years, for example to elucidate the combustion behaviour of iron [73–77], a number of research questions still need to be answered before the overall model can be described in detail. One example is the understanding of the impact of agglomeration and sintering on both the reduction and oxidation process, as it was found to occur during reduction of iron oxides in fluidized bed reactors [78,79]. Another important point is, that due to lack of data the description of the processes is only based on thermodynamic equilibrium calculations and not on kinetics of reduction or oxidation. For a more comprehensive process analysis and development of the technology an accurate

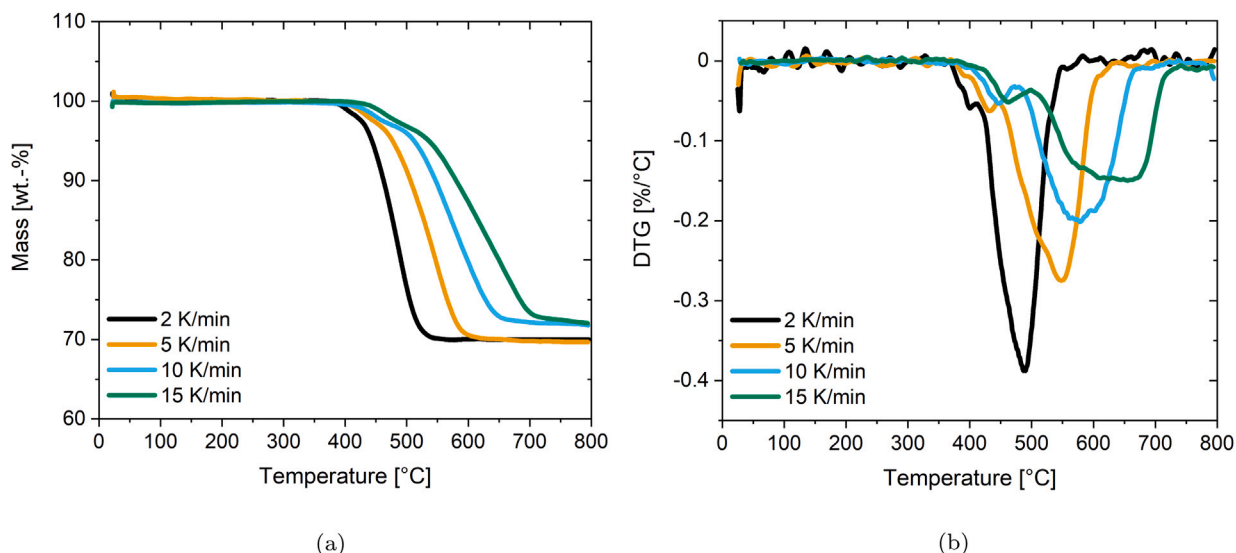


Fig. 8. (a) Thermogravimetric data of the reduction of Fe<sub>2</sub>O<sub>3</sub> with 10% H<sub>2</sub> and varying heating rate and (b) the resulting DTG graphs.

model for iron oxide reduction and oxidation is required. Thus, the next section of this work focuses on the reduction of iron oxide with hydrogen.

#### 4. Experimental results and kinetic analysis

In the experimental section results of the reduction of iron oxides with hydrogen based on thermogravimetric analysis are presented and discussed with respect to the reaction mechanism and kinetic parameters.

##### 4.1. Thermogravimetric analysis

The reduction of iron oxide (Fe<sub>2</sub>O<sub>3</sub>) with hydrogen is investigated based on thermogravimetric analysis. Fig. 8 shows the results of thermogravimetric experiments with 10% H<sub>2</sub> in N<sub>2</sub> and varying heating rates. The overall mass loss is approximately 30% for each heating rate which corresponds to the mass loss due to reduction from Fe<sub>2</sub>O<sub>3</sub> to Fe (30.1%). The deviations of up to 2% from the theoretically achievable mass loss can be attributed to measurement errors due to the buoyancy effect, although a correction measurement was performed for each experiment. The reduction is completed for all heating rates below 800 °C. The reduction starts at  $T = 370$  °C for a heating rate of 2 K min<sup>-1</sup> and is slightly shifted to higher temperatures with increasing heating rate ( $T = 440$  °C with 15 K min<sup>-1</sup>). A more detailed examination of the mass loss graphs shows, that the reduction consists of two well divided stages, which can be seen more clearly in the derivative shown in Fig. 8(b). The first stage ranging from 370 °C to 420 °C for 2 K min<sup>-1</sup> corresponds to a mass loss of approximately 3%. This refers to the reduction of Fe<sub>2</sub>O<sub>3</sub> to Fe<sub>3</sub>O<sub>4</sub> (3.3%) according to Eq. (9). The second stage, consisting of a mass loss of approximately 27% would then correspond to the reduction of Fe<sub>3</sub>O<sub>4</sub> to Fe according to Eq. (10) (26.7%). For a heating rate of 2 K min<sup>-1</sup> the second reduction step ranges from 420 °C to 540 °C. Non-isothermal TGA measurements with various heating rates are characterized by an almost parallel shift of the TGA curve to higher temperatures with increasing heating rate [49].

As can be depicted from Fig. 8, the shift of the experimental curve with increasing heating rate is more pronounced for higher temperatures. The reduction is completed at  $T = 540$  °C for 2 K min<sup>-1</sup> while for 15 K min<sup>-1</sup> the reduction is completed at  $T = 715$  °C. This effect suggests that the reduction might be additionally retarded for high heating rates due to sintering effects that are intensified at higher temperatures [44, 46, 48]. Several authors showed that reduction of Fe<sub>2</sub>O<sub>3</sub> with hydrogen

produces a compact iron layer [44, 46, 48]. The reduction requires diffusion of hydrogen to the iron/iron oxide interface and diffusion of formed water molecules towards the gas phase. The formation of a dense iron layer reduces the diffusion rates of both hydrogen and water and leads to a decrease of the reduction rate at higher temperatures. It is postulated by Kim et al. [80], that the reduction proceeds by diffusion of O-atoms through the dense iron layer to the particle surface, where they react with hydrogen. Reduction leads to a decrease of the BET surface area from 3.37 m<sup>2</sup> g<sup>-1</sup> to 0.74 m<sup>2</sup> g<sup>-1</sup>. A decrease of the specific surface area due to reduction was also investigated by Lee et al. [48] and Hessels et al. [81]. Beside the formation of a dense iron layer this might also be an effect of sintering and pore coalescence. This is confirmed by Hessels et al. [81], who found that with increasing reduction temperature the number of pores decreases and pore size increases. However, delaying the reaction results in better resolution of the reaction steps as can be depicted from the DTG graphs (Fig. 8(b)). It can be clearly seen that the reduction consists of at least two well divided steps. Taking a closer look at the derivatives of 10 K min<sup>-1</sup> and 15 K min<sup>-1</sup> a shoulder on the left side of the second peak (490 °C to 590 °C) could be an indication of an additional reduction step. As the temperatures are above 570 °C, which is the key temperature for FeO stability, the reduction from Fe<sub>3</sub>O<sub>4</sub> to Fe could possibly be further divided in the steps Fe<sub>3</sub>O<sub>4</sub> → FeO and FeO → Fe according to Eqs. (11) and (12).



The influence of varying hydrogen content on the reduction of Fe<sub>2</sub>O<sub>3</sub> was investigated with a heating rate of 2 K min<sup>-1</sup> to prevent sintering effects from superimposing the kinetics. Fig. 9 shows the reduction of Fe<sub>2</sub>O<sub>3</sub> with hydrogen contents of 5%, 10%, 20%, 25% and 30% in the gas phase with a heating rate of 2 K min<sup>-1</sup>. Increasing the hydrogen content leads to a shift of the reduction curve to lower temperatures. The reduction with 10% H<sub>2</sub> starts at 370 °C and is completed at 540 °C while the reduction with 30% H<sub>2</sub> starts at the same temperature but is completed at slightly lower temperatures (500 °C). This implies that higher hydrogen contents lead to an increase of the reaction rate. Comparing the reduction with 20%, 25% and 30%

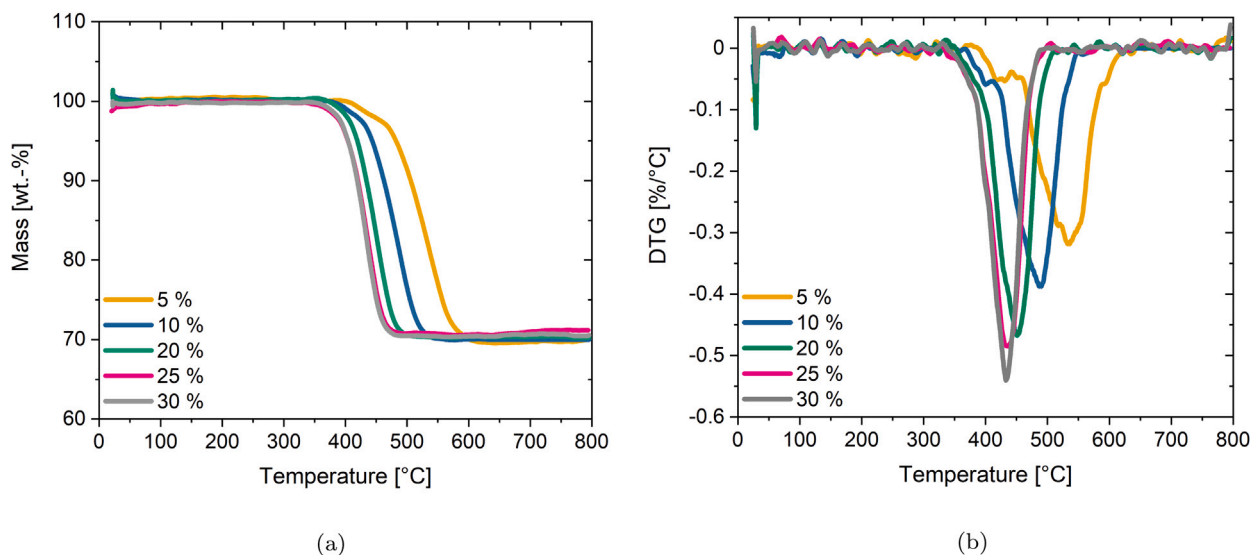


Fig. 9. (a) Experimental data of the reduction of  $\text{Fe}_2\text{O}_3$  with hydrogen contents varying from 5% to 30% and a heating rate of  $2\text{ K min}^{-1}$  and (b) the resulting DTG graphs. For hydrogen contents above 25% a maximum reduction rate is reached.

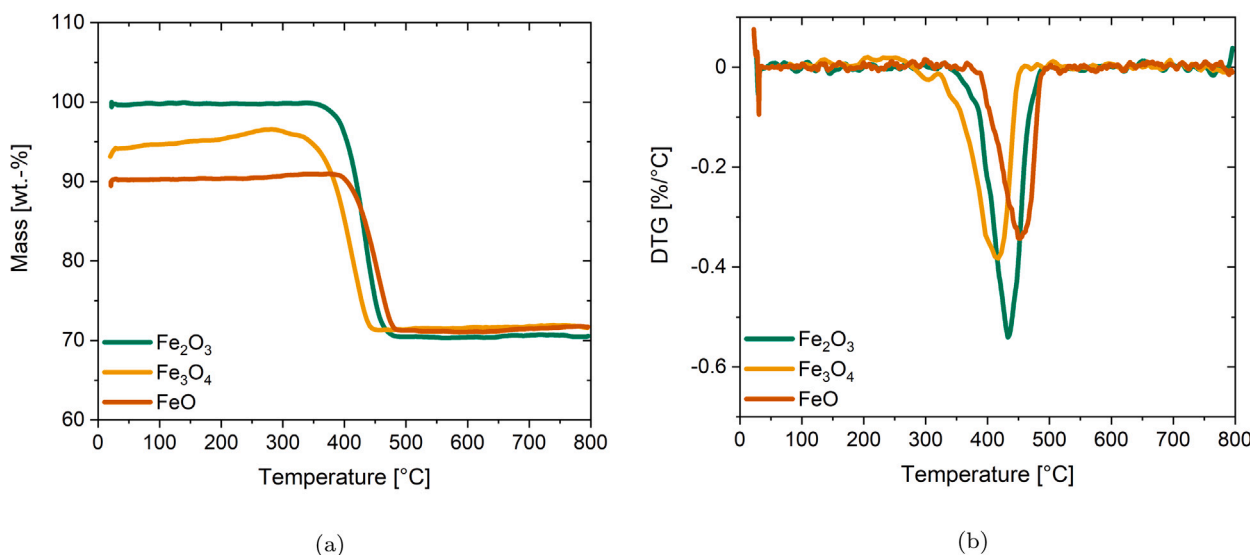


Fig. 10. (a) Thermogravimetric experiments and (b) the resulting DTG graph of the reduction of the oxides  $\text{Fe}_2\text{O}_3$ ,  $\text{Fe}_3\text{O}_4$  and  $\text{FeO}$  with 30%  $\text{H}_2$  in  $\text{N}_2$  and a heating rate of  $2\text{ K min}^{-1}$ .

hydrogen indicates that increasing the hydrogen concentration from 25% to 30% does not lead to a further shift of the TGA curve. This suggests that with a hydrogen content of 25% an equilibrium state is reached. Wimmers et al. [82] and Zieliński et al. [45] demonstrated by TPR experiments that the reduction rate is affected by the amount of gaseous  $\text{H}_2\text{O}$ . They showed that the reduction rate is strongly retarded with increasing water content which is more pronounced for the reduction of  $\text{Fe}_3\text{O}_4$  according to Eq. (10). The retardation of the reaction is not only explained by thermodynamic considerations, e.g. occurrence of the backward reaction, but also by kinetic limitations or blocking of reaction sites [45]. Conversely, this implies that with a hydrogen content of 25% the retardation effects of water vapour which is formed during the reaction are negligible and the maximum reduction rate is reached. In addition to the reduction of  $\text{Fe}_2\text{O}_3$ , the reduction of  $\text{Fe}_3\text{O}_4$  and  $\text{FeO}$  with 30%  $\text{H}_2$  were examined. The resulting TGA graphs and corresponding DTG curves are shown in Fig. 10.

For better comparability  $\text{Fe}_3\text{O}_4$  and  $\text{FeO}$  TGA curves are depicted according to the theoretically expected mass losses of the reduction sequence  $\text{Fe}_2\text{O}_3 \rightarrow \text{Fe}_3\text{O}_4 \rightarrow \text{FeO}$ . For all three oxides reduction is

completed for temperatures around 500°C. The start of the reduction differs slightly for the oxides but is in the same temperature range. The reduction of  $\text{Fe}_3\text{O}_4$  starts at 340°C. The reduction of  $\text{Fe}_2\text{O}_3$  starts at 370°C and the reduction of  $\text{FeO}$  at 395°C. Although the BET area of the  $\text{FeO}$  sample is smaller ( $0.26\text{ m}^2\text{ g}^{-1}$ ) than of the  $\text{Fe}_3\text{O}_4$  ( $2.44\text{ m}^2\text{ g}^{-1}$ ) and  $\text{Fe}_2\text{O}_3$  ( $3.37\text{ m}^2\text{ g}^{-1}$ ) powder samples, it seems not to have a decisive influence on the reduction progress at this high hydrogen contents. This might be due to the high diffusivity of hydrogen. The development of the reduction of  $\text{Fe}_2\text{O}_3$ ,  $\text{Fe}_3\text{O}_4$  and  $\text{FeO}$  is comparable as an almost parallel shift over the complete temperature range can be observed. For the oxides  $\text{Fe}_3\text{O}_4$  and  $\text{FeO}$  only one reduction step can be detected. This underlines that the reduction of  $\text{Fe}_2\text{O}_3$  is divided in two steps whereas the first step can be characterized as reduction to  $\text{Fe}_3\text{O}_4$  (Eq. (9)). The second step cannot be further defined based on the experimental data, as the reduction curves do not show any characteristic features which would indicate an additional reduction step. However, a multistep reduction of the second step cannot be excluded as overlapping of reactions may occur. Additionally, the occurrence of  $\text{FeO}$  in the  $\text{Fe}_3\text{O}_4$  reduction process due to comproportionation or the corresponding

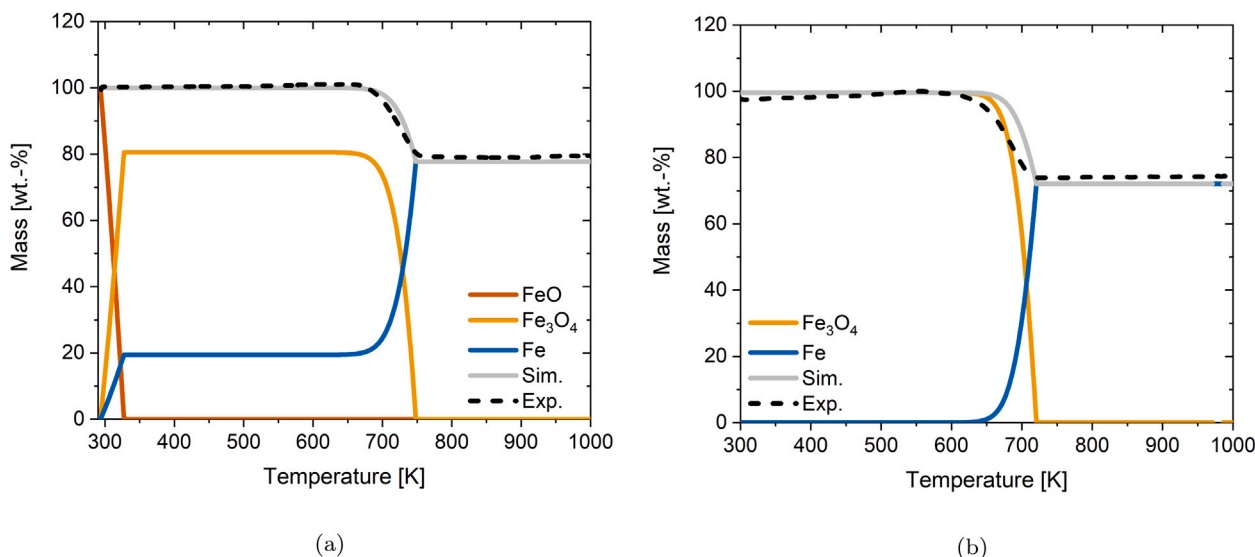


Fig. 11. Simulation and experiment of (a) FeO reduction with 30% H<sub>2</sub> (100 mL min<sup>-1</sup>, 2 K min<sup>-1</sup>) and (b) Fe<sub>3</sub>O<sub>4</sub> reduction with 30% H<sub>2</sub> (100 mL min<sup>-1</sup>, 2 K min<sup>-1</sup>).

disproportionation of FeO to Fe<sub>3</sub>O<sub>4</sub> and Fe is not characterized by a loss of mass.

#### 4.2. Reaction mechanism and simulations

For kinetic analysis the experimental results presented in Section 4.1 are simulated with the software package DETCHEM<sup>MPTR</sup>, which is described in Section 2.3. Based on the experimental results and literature predictions a reaction mechanism for iron oxide reduction with hydrogen was developed. In a previous analysis it could be shown that the particle size ( $d_p < 20 \mu\text{m}$  to  $d_p > 67 \mu\text{m}$ ) has no influence on the reduction behaviour (s. Section 2.2). Therefore, it is concluded that transport limitations can be neglected. It is assumed that the reduction of Fe<sub>2</sub>O<sub>3</sub> is a three step mechanism with Fe<sub>3</sub>O<sub>4</sub> and FeO as intermediate products according to Eqs. (9), (11) and (12). FeO is assumed to be an intermediate product although it might not be formed for all experimental conditions. However, the aim of this work is the development of a reaction scheme adaptable for a wide range of conditions. Thus, FeO as intermediate cannot be neglected. To ensure stability of FeO solely for temperatures above 570 °C the decomposition of FeO to Fe<sub>3</sub>O<sub>4</sub> and Fe is given as an equilibrium reaction according to Eq. (13). It should be noted that the underlying kinetics are not based on experimental data but solely on the requirement that FeO is not stable for  $T < 570 \text{ °C}$ .



Kinetic analysis was performed iteratively, starting with FeO. The kinetic model considers the specific surface area of the oxides used (s. Section 2.3). It is therefore assumed that the influence of the specific surface on the reduction rate, and thus the kinetic parameters, is represented by the kinetic model. This allows the inclusion of all oxides in the model, despite their different morphologies. The comparison between simulation and experimental results is shown in Fig. 11(a). FeO reduction follows a two step reaction according Eqs. (12) and (13) and shows good agreement between simulation and experiment. The reaction rate of FeO disproportionation might be slower than depicted within the simulation due to lack of data. Further experimental data e.g. DSC would be necessary for an accurate description. For simulation of Fe<sub>3</sub>O<sub>4</sub> reduction both steps according to Eqs. (11) and (12) as well as Eq. (13) are taken into account. In Fig. 11(b) both the experimental and the simulation results are depicted. It can be seen that Fe<sub>3</sub>O<sub>4</sub> reduction appears to be a one step reduction for these experimental conditions (2 K min<sup>-1</sup> and 30% H<sub>2</sub>) as no FeO is formed. This is in agreement

with experimental results by Zieliński et al. [45] who postulate Fe<sub>3</sub>O<sub>4</sub> reduction as one step process for high H<sub>2</sub> contents.

For the complete description of Fe<sub>2</sub>O<sub>3</sub> reduction Eq. (9) is taken into account in addition to Eqs. (11)–(13). As described above and shown in Fig. 9 increasing the hydrogen content accelerates the reduction process since the influence of the backwards reaction decreases. Thus, for the complete description of Fe<sub>2</sub>O<sub>3</sub> reduction, both the backwards reaction for Fe<sub>3</sub>O<sub>4</sub> and FeO reduction according to Eqs. (14) and (15) are taken additionally into account. The influence of the backwards reaction is negligible for FeO and Fe<sub>3</sub>O<sub>4</sub> reduction according to Fig. 11 due to the high hydrogen content. The backwards reaction of Fe<sub>2</sub>O<sub>3</sub> reduction (Eq. (9)) is not considered as it was shown by Lorente et al. [83], that it is nearly irreversible.



Fig. 12 shows the experimental and simulation results of the reduction of Fe<sub>2</sub>O<sub>3</sub> with 5% and 30% hydrogen and the predicted formation of the intermediate reaction products Fe<sub>3</sub>O<sub>4</sub> and FeO. The retardation of the reduction process due to an increased H<sub>2</sub>O to H<sub>2</sub> ratio is well predictable with the kinetic data. The simulations show, that for 5% hydrogen three reduction steps Fe<sub>2</sub>O<sub>3</sub> → Fe<sub>3</sub>O<sub>4</sub> → FeO → Fe can be distinguished whereas for higher hydrogen contents FeO reduction is very fast and thus formation of FeO is not observed. This shows that the hydrogen content does not only affect the reaction velocity but also the apparent reaction mechanism. This is in contrast to several authors who state solely the temperature as crucial point for FeO formation [41,46,47].

To analyse whether further increasing the hydrogen content accelerates the reduction velocity, simulations were performed with 5% to 100% H<sub>2</sub>. It can be shown that increasing the hydrogen content from 30% to 100% causes only a small increase in the reaction rate (s. supplementary material). For further validation of the postulated reaction mechanism and kinetic data, simulations were also performed for experiments with varying heating rates according to the experiments shown in Fig. 8(b). As described above increasing the heating rate leads to a strong shift of the TGA curve to higher temperatures, especially for the second reduction step. Based on the simulations it can be shown that this is not only an effect of sintering processes but also of the deceleration of Fe<sub>3</sub>O<sub>4</sub> reduction and the formation of FeO due to the backwards reactions which play a more important role at lower residence times (Fig. 13). The predicted mechanism and kinetic data

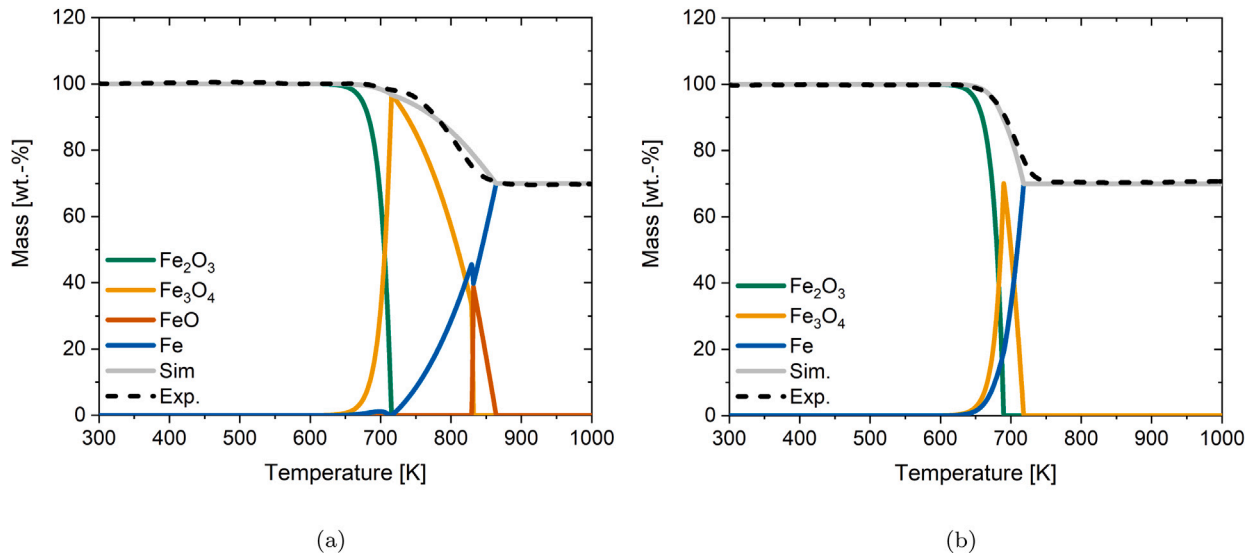


Fig. 12. Experimental results and simulation of thermogravimetric analysis of  $\text{Fe}_2\text{O}_3$  reduction with a heating rate of  $2 \text{ K min}^{-1}$  and (a) 5% and (b) 30%  $\text{H}_2$ .

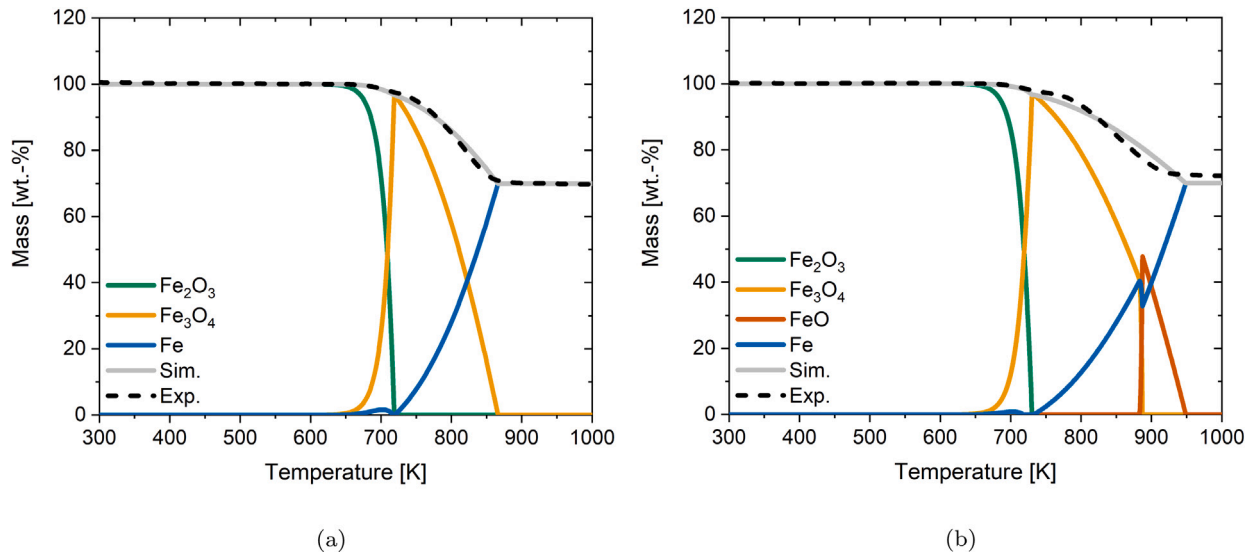


Fig. 13. Experimental results and simulation of thermogravimetric analysis of  $\text{Fe}_2\text{O}_3$  reduction with 10%  $\text{H}_2$  and (a)  $5 \text{ K min}^{-1}$  and (b)  $10 \text{ K min}^{-1}$  heating rate.

show good agreement for all heating rates (s. supplementary material). All simulations were conducted with the kinetic data summarized in Table 6. A comparison between the thermodynamic equilibrium calculations and kinetic simulations shows good agreement, although deviations can be observed for small  $\lambda_{\text{red}}$  and high reduction temperatures (s. supplementary material). The model presented in this work is a global kinetic model. This model will be further developed to a microkinetic model in the future. This includes e.g. the resolution of the reactions into elementary steps but also the consideration of solid phase diffusion, e.g. diffusion of oxygen atoms over vacancies in the lattice.

## 5. Conclusion

In this work, the feasibility of iron as energy carrier is investigated. An analysis of the overall energy cycle was conducted. Based on equilibrium calculations with the simulation software AspenPlus® the efficiency of the reduction process is predicted to be 91% and 43% of the oxidation process. With a hydrogen production efficiency of 70% this results in an overall cycle efficiency of 27%. For a more

Table 6

Kinetic parameters (Activation Energy  $E_{a,k}$ , Arrhenius parameter  $A_k$  and reaction order  $n_{i,k}$ ) of the proposed reaction scheme of  $\text{Fe}_2\text{O}_3$  reduction with  $\text{H}_2$ .

Reaction	$n_{i,k}$	$A_k$	$E_{a,k} [\text{kJ mol}^{-1}]$
$3 \text{ Fe}_2\text{O}_3 + 4 \text{ H}_2 \rightarrow 2 \text{ Fe}_3\text{O}_4 + 4 \text{ H}_2\text{O}$	1 + 1	$2 \cdot 10^{10}$	282
$\text{Fe}_3\text{O}_4 + \text{H}_2 \rightarrow 3 \text{ FeO} + \text{H}_2\text{O}$	1 + 1	$8.5 \cdot 10^9$	280
$3 \text{ FeO} + \text{H}_2\text{O} \rightarrow \text{Fe}_3\text{O}_4 + \text{H}_2$	1 + 1	$2.2 \cdot 10^7$	235
$\text{FeO} + \text{H}_2 \rightarrow \text{Fe} + \text{H}_2\text{O}$	1 + 1.8	$3 \cdot 10^{10}$	285
$\text{Fe} + \text{H}_2\text{O} \rightarrow \text{FeO} + \text{H}_2$	1 + 1.2	$6.5 \cdot 10^7$	231
$4 \text{ FeO} \rightleftharpoons \text{Fe}_3\text{O}_4 + \text{Fe}$	4	$5 \cdot 10^{-24}$	7

comprehensive process analysis and development of the technology an accurate reaction kinetic model for iron oxide reduction and oxidation is required. Thus, the reduction of iron oxide with hydrogen was investigated based on thermogravimetric experiments. It could be shown that the reduction process can be divided in two stages. The reduction of  $\text{Fe}_2\text{O}_3$  to  $\text{Fe}_3\text{O}_4$  and the reduction of  $\text{Fe}_3\text{O}_4$  to Fe, where FeO might be an intermediate product. Based on the experimental results a reaction mechanism and the associated kinetic data for  $\text{Fe}_2\text{O}_3$  reduction with hydrogen is postulated. It is assumed that the reduction of  $\text{Fe}_2\text{O}_3$  is

a three-step process with  $\text{Fe}_3\text{O}_4$  and  $\text{FeO}$  as intermediate products. In addition, it was demonstrated that the backwards reactions of  $\text{Fe}_3\text{O}_4$  and  $\text{FeO}$  reduction have a decisive influence on the course of the reaction and the apparent reaction mechanism. For further verification of the mechanism additional investigations e.g. by differential scanning calorimetry, in situ XRD or analysis of intermediate reduction steps are of high interest and will be addressed in future. The predicted model needs to be further refined regarding the effect of sintering and the resulting change of the surface area during the course of the reduction as well as transport limitations that might occur. The influence of the backwards reactions is an important factor, that needs to be considered in a detailed description of the reduction process. In a more detailed case study it is recommended to determine which kind of reactor, e.g. fluidized bed, blast-furnace or rotary drum reactor is the most promising. Beside the reduction, elucidation of the oxidation kinetics is also an important task that will be addressed in future research.

### Declaration of competing interest

The authors declare that they have no known competing financial interests or personal relationships that could have appeared to influence the work reported in this paper.

### Data availability

Data will be made available on request.

### Acknowledgements

This work was performed within the cluster project Clean Circles. Financial support by the Strategy Fund of the KIT Presidium is gratefully acknowledged. Furthermore, we acknowledge Steinbeis GmbH & Co. KG für Technologietransfer (STZ 240 Reaktive Strömung) for a cost-free license of DETCHEM.

### Appendix A. Supplementary data

Supplementary material related to this article can be found online at <https://doi.org/10.1016/j.jaecs.2022.100096>.

### References

- [1] UN. The Paris agreement. 2015, URL: <https://unfccc.int/documents/37107>.
- [2] UN. Glasgow climate pact. 2021, URL: <https://unfccc.int/documents/310475>.
- [3] International Energy Agency. Global energy and CO<sub>2</sub> status report: The latest trends in energy and emissions in 2018. IEA Publications; 2019.
- [4] International Energy Agency. Key world energy statistics. IEA Publications; 2021.
- [5] Dunn B, Kamath H, Tarascon J-M. Electrical energy storage for the grid: a battery of choices. *Science* 2011;334(6058):928–35.
- [6] Sterner M, Stadler I. *Energiespeicher - Bedarf, Technologien, Integration*. Berlin, Heidelberg: Springer Berlin Heidelberg; 2014, <http://dx.doi.org/10.1007/978-3-642-37380-0>.
- [7] Möller KT, Jensen TR, Akiba E, Li HW. Hydrogen - A sustainable energy carrier. *Prog Nat Sci: Mater Int* 2017;27(1):34–40.
- [8] Mazloomi K, Gomes C. Hydrogen as an energy carrier: Prospects and challenges. *Renew Sustain Energy Rev* 2012;16(5):3024–33.
- [9] Andersson J, Grönkvist S. Large-scale storage of hydrogen. *Int J Hydrog Energy* 2019;44(23):11901–19.
- [10] Bergthorson JM. Recyclable metal fuels for clean and compact zero-carbon power. *Prog Energy Combust Sci* 2018;68:169–96.
- [11] Auner N, Holl S. Silicon as energy carrier—Facts and perspectives. *Energy* 2006;31(10–11):1395–402.
- [12] Lott P, Deutschmann O. Heterogeneous chemical reactions—A cornerstone in emission reduction of local pollutants and greenhouse gases. *Proc Combust Inst* 2022.
- [13] Dirven L, Deen NG, Golombok M. Dense energy carrier assessment of four combustible metal powders. *Sustain Energy Technol* 2018;30:52–8.
- [14] Mignard D, Pritchard C. A review of the sponge iron process for the storage and transmission of remotely generated marine energy. *Int J Hydrog Energy* 2007;32(18):5039–49.
- [15] Shkolnikov EI, Zhuk AZ, Vlaskin MS. Aluminum as energy carrier: Feasibility analysis and current technologies overview. *Renew Sustain Energy Rev* 2011;15(9):4611–23.
- [16] Trowell KA, Goroshin S, Frost DL, Bergthorson JM. Aluminum and its role as a recyclable, sustainable carrier of renewable energy. *Appl Energy* 2020;275:115112.
- [17] Julien P, Bergthorson JM. Enabling the metal fuel economy: green recycling of metal fuels. *Sustain Energy Fuels* 2017;1(3):615–25.
- [18] Bardsley WE. The sustainable global energy economy: Hydrogen or silicon? *Nat Resour Res* 2008;17(4):197–204.
- [19] Theoretical energy release of thermites, intermetallics, and combustible metals. 1998, <http://dx.doi.org/10.2172/658208>.
- [20] Demirbas A. Combustion characteristics of different biomass fuels. *Prog Energy Combust Sci* 2004;30(2):219–30.
- [21] Zamfirescu C, Dincer I. Using ammonia as a sustainable fuel. *J Power Sources* 2008;185(1):459–65.
- [22] Li Y, Chen H, Zhang X, Tan C, Ding Y. Renewable energy carriers: Hydrogen or liquid air/nitrogen? *Appl Therm Eng* 2010;30(14–15):1985–90.
- [23] Bergthorson JM, Goroshin S, Soo MJ, Julien P, Palecka J, Frost DL, Jarvis DJ. Direct combustion of recyclable metal fuels for zero-carbon heat and power. *Appl Energy* 2015;160:368–82.
- [24] Wiinikka H, Vikström T, Wennebro J, Toth P, Sepman A. Pulverized sponge iron, a zero-carbon and clean substitute for fossil coal in energy applications. *Energy Fuels* 2018;32(9):9982–9.
- [25] Tóth P, Ögren Y, Sepman A, Gren P, Wiinikka H. Combustion behavior of pulverized sponge iron as a recyclable electrofuel. *Powder Technol* 2020;373:210–9.
- [26] Gupta A, Basu B. Sustainable primary aluminium production: Technology status and future opportunities. *Trans Indian Inst Met* 2019;72(8):2135–50.
- [27] Alamdari H. Aluminium production process: Challenges and opportunities. *Metals* 2017;7(4):133.
- [28] Allanore A. Features and challenges of molten oxide electrolytes for metal extraction. *J Electrochem Soc* 2015;162(1):E13–22.
- [29] Nohira T, Yasuda K, Ito Y. Pinpoint and bulk electrochemical reduction of insulating silicon dioxide to silicon. *Nature Mater* 2003;2(6):397–401.
- [30] Wang D, Jin X, Chen GZ. Solid state reactions: an electrochemical approach in molten salts. *Annu Rep Prog Chem Sect C: Phys Chem* 2008;104:189–234.
- [31] Wang Q, Zhu Y, Wu Q, Gratz E, Wang Y. Low temperature electrolysis for iron production via conductive colloidal electrode. *RSC Adv* 2015;5(8):5501–7.
- [32] Allanore A, Lavelaine H, Valentin G, Birat JP, Delcroix P, Lapique F. Observation and modeling of the reduction of hematite particles to metal in alkaline solution by electrolysis. *Electrochim Acta* 2010;55(12):4007–13.
- [33] Zou X, Gu S, Lu X, Xie X, Lu C, Zhou Z, Ding W. Electroreduction of iron(III) oxide pellets to iron in alkaline media: A typical shrinking-core reaction process. *Metall Mater Trans B* 2015;46(3):1262–74.
- [34] Miller MA, Wainright JS, Savinell RF. Iron electrodeposition in a deep eutectic solvent for flow batteries. *J Electrochem Soc* 2017;164(4):A796–803.
- [35] Bhaskar A, Assadi M, Nikpey Somehsaraei H. Decarbonization of the iron and steel industry with direct reduction of iron ore with green hydrogen. *Energies* 2020;13(3):758.
- [36] Nuber D, Eichberg H, Rollinger B. Circored fine ore direct reduction - the future of modern electric steel making. *Stahl Eisen* 2006;(126):47–51.
- [37] Vogl V, Åhman M, Nilsson LJ. Assessment of hydrogen direct reduction for fossil-free steelmaking. *J Clean Prod* 2018;203:736–45.
- [38] Pei M, Petäjäniemi M, Regnell A, Wijk O. Toward a fossil free future with HYBRIT: Development of iron and steelmaking technology in Sweden and Finland. *Metals* 2020;10(7):972.
- [39] Angeli SD, Gossler S, Lichtenberg S, Kass G, Agrawal AK, Valerius M, Kinzel KP, Deutschmann O. Reduction of CO<sub>2</sub> emission from off-gases of steel industry by dry reforming of methane. *Angew Chem Int Ed* 2021;60(21):11852–7.
- [40] Spreitzer D, Schenk J. Reduction of iron oxides with hydrogen—A review. *Steel Res Int* 2019;90(10):1900108.
- [41] Jozwiak WK, Kaczmarek E, Maniecki TP, Ignaczak W, Maniukiewicz W. Reduction behavior of iron oxides in hydrogen and carbon monoxide atmospheres. *Appl Catal A* 2007;326(1):17–27.
- [42] Wang Y, Wang X, Hua X, Zhao C, Wang W. The reduction mechanism and kinetics of Fe<sub>2</sub>O<sub>3</sub> by hydrogen for chemical-looping hydrogen generation. *J Therm Anal Calorim* 2017;129(3):1831–8.
- [43] Abu Tahari MN, Salleh F, Tengku Saharuddin TS, Dzakarria N, Samsuri A, Mohamed Hisham MW, Yarmo MA. Influence of hydrogen and various carbon monoxide concentrations on reduction behavior of iron oxide at low temperature. *Int J Hydrog Energy* 2019;44(37):20751–9.
- [44] Pourghahramani P, Forsberg E. Reduction kinetics of mechanically activated hematite concentrate with hydrogen gas using nonisothermal methods. *Thermochim Acta* 2007;454(2):69–77.
- [45] Zieliński J, Zglinicka I, Znak L, Kaszkur Z. Reduction of Fe<sub>2</sub>O<sub>3</sub> with hydrogen. *Appl Catal A* 2010;381(1–2):191–6.
- [46] Pineau A, Kanari N, Gaballah I. Kinetics of reduction of iron oxides by H<sub>2</sub>: Part II. Low temperature reduction of magnetite. *Thermochim Acta* 2007;456(2):75–88.

- [47] Pineau A, Kanari N, Gaballah I. Kinetics of reduction of iron oxides by H<sub>2</sub>: Part I: Low temperature reduction of hematite. *Thermochim Acta* 2006;447(1):89–100.
- [48] Lee G-Y, Song J-I, Lee J-S. Reaction kinetics and phase transformation during hydrogen reduction of spherical Fe<sub>2</sub>O<sub>3</sub> nanopowder agglomerates. *Powder Technol* 2016;302:215–21.
- [49] Vyazovkin S, Chrissafis K, Di Lorenzo ML, Koga N, Pijolat M, Roduit B, Sbirrazzuoli N, Suñol JJ. ICTAC Kinetics Committee recommendations for collecting experimental thermal analysis data for kinetic computations. *Thermochim Acta* 2014;590:1–23.
- [50] Allelein H-J, Bollin E, Schelling U, Schwarz H, Wörsdörfer D. *Energietechnik: Systeme zur konventionellen und erneuerbaren Energieumwandlung. Kompaktwissen für Studium und Beruf*. 8th ed.. Lehrbuch, Wiesbaden: Springer Vieweg; 2019.
- [51] Nazarko Y. *Energetische und wirtschaftliche Optimierung eines membranbasierten Oxyfuel-Dampfkraftwerkes* (Ph.D. thesis), Aachen: RWTH Aachen University; 2015.
- [52] Bundesnetzagentur Germany. Power plant list. 2021, URL: <https://www.bundesnetzagentur.de/EN/Areas/Energy/Companies/SecurityOfSupply/GeneratingCapacity/PowerPlantList/start.html;jsessionid=CDDBF7A641A5E50BA29F7328B8F22C8>.
- [53] aus der Wiesche S, Joos F. *Handbuch Dampfturbinen: Grundlagen, Konstruktion, Betrieb*. Wiesbaden and Heidelberg: Springer Vieweg; 2018, <http://dx.doi.org/10.1007/978-3-658-20630-7>.
- [54] Green DW, Perry RH. *Perry's chemical engineers' handbook*. McGraw-Hill's accessengineering, 8th ed.. New York: McGraw-Hill; 2008, <http://dx.doi.org/10.1036/0071511245>.
- [55] Schuknecht M. *Entwicklungspotential eines Kombikraftwerks mit Druckkohlenstaubfeuerung* (Ph.D. thesis), Essen: Universität Essen; 2003.
- [56] Strauß K. *Kraftwerkstechnik: Zur Nutzung fossiler, nuklearer und regenerativer Energiequellen*. VDI-Buch, 7th ed.. Berlin and Heidelberg: Springer Vieweg; 2016, <http://dx.doi.org/10.1007/978-3-662-53030-6>.
- [57] Deutschmann O, Tischer S, Correa C, Chatterjee D, Kleditzsch S, Janardhanan VM, Mladenov N, Minh HD, Karadeniz H, Hettel M, Menon V, Banerjee A, Goßler H, Daymo E. DETCHEM software package. 2020, URL: [www.detchem.com](http://www.detchem.com).
- [58] Tischer S, Börnhorst M, Amsler J, Schoch G, Deutschmann O. Thermodynamics and reaction mechanism of urea decomposition. *Phys Chem Chem Phys* 2019;21(30):16785–97.
- [59] Kuntz C, Kuhn C, Weickenmeier H, Tischer S, Börnhorst M, Deutschmann O. Kinetic modeling and simulation of high-temperature by-product formation from urea decomposition. *Chem Eng Sci* 2021;246:116876.
- [60] Goos E, Burcat A, Ruscic B. Extended third millennium ideal gas and condensed phase thermochemical database for combustion with updates from active thermochemical tables. 2010, URL: [https://www.dlr.de/vt/desktopdefault.aspx/tabid-7603/12862\\_read-32379/](https://www.dlr.de/vt/desktopdefault.aspx/tabid-7603/12862_read-32379/).
- [61] Debiagi P, Rocha RC, Scholtissek A, Janicka J, Hasse C. Iron as a sustainable chemical carrier of renewable energy: Analysis of opportunities and challenges for retrofitting coal-fired power plants. *Renew Sustain Energy Rev* 2022;165:112579.
- [62] Ausfelder F, Beilmann C, Bertau M, Bräuninger S, Heinzel A, Hoer R, Koch W, Mahlendorf F, Metzelthin A, Peuckert M, Plass L, Röchle K, Reuter M, Schaub G, Schiebahn S, Schwab E, Schüth F, Stolten D, Tefßmer G, Wagemann K, Ziegahn KF. *Energiespeicherung als Element einer sicheren Energieversorgung*. *Chem Ing Tech* 2015;87(1–2):17–89.
- [63] Wijayanta AT, Oda T, Purnomo CW, Kashiwagi T, Aziz M. Liquid hydrogen, methylcyclohexane, and ammonia as potential hydrogen storage: Comparison review. *Int J Hydrog Energy* 2019;44(29):15026–44.
- [64] Aasadnia M, Mehrpooya M. Large-scale liquid hydrogen production methods and approaches: A review. *Appl Energy* 2018;212:57–83.
- [65] Cigolotti V, Genovese M, Fragiaco P. Comprehensive review on fuel cell technology for stationary applications as sustainable and efficient poly-generation energy systems. *Energies* 2021;14(16):4963.
- [66] Peters R, Deja R, Engelbracht M, Frank M, van Nguyen N, Blum L, Stolten D. Efficiency analysis of a hydrogen-fueled solid oxide fuel cell system with anode off-gas recirculation. *J Power Sources* 2016;328:105–13.
- [67] Sanz W, Braun M, Jericha H, Platzer MF. Adapting the zero-emission Graz Cycle for hydrogen combustion and investigation of its part load behavior. *Int J Hydrog Energy* 2018;43(11):5737–46.
- [68] Giddey S, Badwal SPS, Munnings C, Dolan M. Ammonia as a renewable energy transportation media. *ACS Sustain Chem Eng* 2017;5(11):10231–9.
- [69] Institute for Sustainable Process Technology. *Power to ammonia: Feasibility study for the value chains and business cases to produce CO<sub>2</sub>-free ammonia suitable for various market applications*. 2017, URL: <https://topsectorenergie.nl/sites/default/files/uploads/Energie%20en%20Industrie/Power%20to%20Ammonia%202017.pdf>.
- [70] Kishimoto M, Muroyama H, Suzuki S, Saito M, Koide T, Takahashi Y, Horiuchi T, Yamasaki H, Matsumoto S, Kubo H, Takahashi N, Okabe A, Ueguchi S, Jun M, Tateno A, Matsuo T, Matsui T, Iwai H, Yoshida H, Eguchi K. Development of 1 kW-class ammonia-fueled solid oxide fuel cell stack. *Fuel Cells* 2020;20(1):80–8.
- [71] EnBW. *Rheinhafen-Dampfkraftwerk Karlsruhe*. 2021, URL: <https://www.enbw.com/unternehmen/konzern/energieerzeugung/neubau-und-projekte/rheinhafen-dampfkraftwerk-karlsruhe/technik.html#content-navigation>.
- [72] Goto K, Yogo K, Higashii T. A review of efficiency penalty in a coal-fired power plant with post-combustion CO<sub>2</sub> capture. *Appl Energy* 2013;111:710–20.
- [73] Goroshin S, Tang F-D, Higgins AJ, Lee JH. Laminar dust flames in a reduced-gravity environment. *Acta Astronaut* 2011;68(7–8):656–66.
- [74] Ning D, Shoshin Y, van Stiphout M, van Oijen J, Finotello G, de Goey P. Temperature and phase transitions of laser-ignited single iron particle. *Combust Flame* 2022;236:111801.
- [75] Tang F-D, Goroshin S, Higgins AJ. Modes of particle combustion in iron dust flames. *Proc Combust Inst* 2011;33(2):1975–82.
- [76] Choisez L, van Rooij NE, Hessels CJ, Da Silva AK, Filho IRS, Ma Y, de Goey P, Springer H, Raabe D. Phase transformations and microstructure evolution during combustion of iron powder. *Acta Mater* 2022;239:118261.
- [77] Hazenberg T, van Oijen JA. Structures and burning velocities of flames in iron aerosols. *Proc Combust Inst* 2021;38(3):4383–90.
- [78] Zhong Y-W, Wang Z, Gong X-Z, Guo Z-C. Sticking behavior caused by sintering in gas fluidisation reduction of hematite. *Ironmak Steelmak* 2012;39(1):38–44.
- [79] Komatina M, Gudenau HW. The sticking problem during direct reduction of fine iron ore in the fluidized bed. *Metall Mater Eng* 2004;10(4):309–28.
- [80] Kim S-H, Zhang X, Ma Y, Souza Filho IR, Schweinar K, Angenendt K, Vogel D, Stephenson LT, El-Zoka AA, Mianroodi JR, Rohwerder M, Gault B, Raabe D. Influence of microstructure and atomic-scale chemistry on the direct reduction of iron ore with hydrogen at 700 °C. *Acta Mater* 2021;212:116933.
- [81] Hessels C, Homan T, Deen NG, Tang Y. Reduction kinetics of combusted iron powder using hydrogen. *Powder Technol* 2022;407:117540.
- [82] Wimmers OJ, Arnoldy P, Mouljin PA. Determination of the reduction mechanism by temperature-programmed reduction: Application to small Fe<sub>2</sub>O<sub>3</sub> particles. *J Phys Chem* 1986;90:1331–7.
- [83] Lorente E, Herguido J, Peña JA. Steam-iron process: Influence of steam on the kinetics of iron oxide reduction. *Int J Hydrog Energy* 2011;36(21):13425–34.